MDPI

Article

The Aerodynamics of an Iron Ore Pelletizing Rotary Kiln

I. A. Sofia Larsson ⓘ

Fluid Mechanics, Department of Engineering Sciences and Mathematics, Luleå University of Technology, SE-97181 Luleå, Sweden; sofia.larsson@ltu.se

Abstract: This paper summarizes more than a decade of systematic studies of the flow field in an iron ore pelletizing rotary kiln using computational fluid dynamics (CFD) on simplified models of a real kiln. Physical, laser-based experiments have been performed to validate part of the numerical results. The objective is a better understanding of the kiln aerodynamics and, by extension, its effect on the combustion process. Despite all of the simplifications regarding the models studied in this project, the results show the importance of correctly predicting the flow field in order to optimize the combustion process. Combustion simulations revealed that the heat release from the flame does not affect or change the flow field in any significant way; the flow field, however, governs the flame propagation and affects the combustion process by controlling the mixing rates of fuel and air. Using down-scaled isothermal water models for investigating kiln aerodynamics in general and mixing properties in particular is therefore justified. Although the heat release from the flame cannot be accounted for in isothermal models, valuable implications regarding the real process can still be gained. To better model the actual process numerically, more advanced submodels for both the combustion and especially the flow field are needed. The complex flow field in this type of rotary kiln requires a careful choice of turbulence model to obtain accurate simulation results.

Keywords: rotary kiln; kiln aerodynamics; turbulence; mixing; combustion; CFD; experiments

1. Introduction

The pelletizing process, where the crude ore from the mine is upgraded, involves several steps, including grinding, balling, and induration; see Figure 1 to the left. In the grate-kiln induration process [1]—see Figure 1 to the right—the sintering is mainly taking place in a rotary kiln, where the pellets increase their strength and metallurgical properties. The kiln comprises a large, cylindrical, rotating oven with a burner in one end producing a diffusion flame providing the necessary heat throughout the whole kiln and to the earlier stages of the process. Maintaining a proper heat profile throughout the kiln is paramount to obtaining the highest quality of pellets produced.
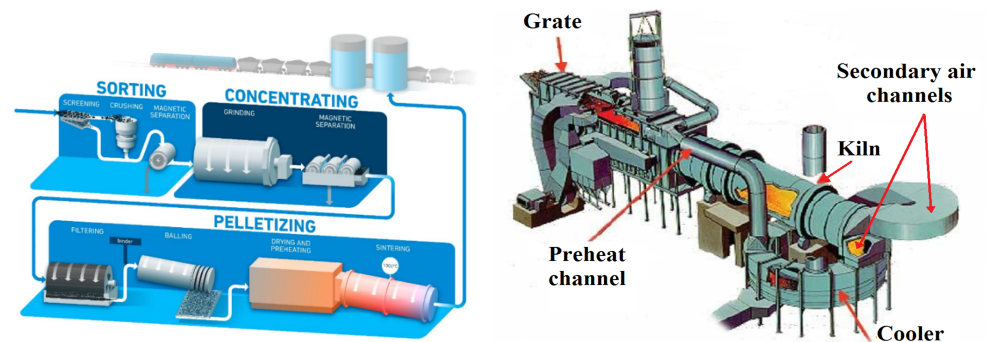

Figure 1. Production of iron ore pellets, process overview to the left, and grate–kiln indurating machine to the right. Courtesy of Luossavaara-Kiirunavaara Aktiebolag (LKAB).

The international mining and minerals group Luossavaara-Kiirunavaara Aktiebolag (LKAB) in Sweden is one of the world's leading producers of highly upgraded iron ore products, including pellets. LKAB's kilns are about 5–7 m in diameter and 35–43 m long and differ from kilns used in other industrial processes in both geometry and operating conditions. The crude ore in the mine consists mostly of magnetite, which, in the pelletizing process, oxidizes to hematite, releasing a large amount of energy that is supplied back into the process as heat. As much as two-thirds of the energy required originates from the oxidation. A large amount of process gas, supplied through the kiln, is therefore necessary in the process for complete oxidation to occur.

The process gas, consisting of air (called secondary air) both for the combustion and the oxidation of the pellets, is supplied through the kiln hood; see Figure 2. There are two inlets for the secondary air and in between the dividing wall, called the backplate; the 50 MW burner is located where the primary air and the fuel (currently pulverized coal) enters. As a comparison, the kiln of interest in this work has a mass flow ratio of secondary to primary air of approximately twice that of typical cement kilns and more than four times that of typical lime kilns. Relating the airflow to the fuel flow, an air-to-fuel equivalence ratio of 4–6 is obtained in the kiln [2].
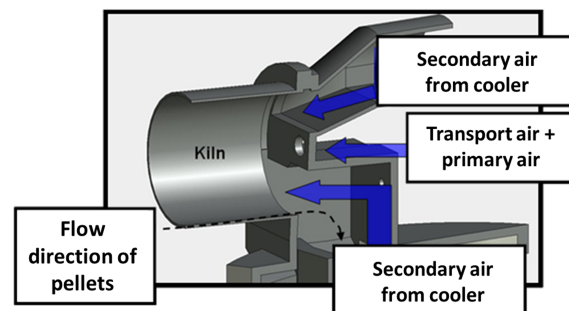

Figure 2. One of the two types of kiln hoods used in LKAB's pelletizing processes, this geometry has been the main focus of the work presented here. Courtesy of LKAB.

The secondary air is hot with a high oxygen/fuel ratio, and hence has a substantial momentum. To enable combustion, the co-flowing air needs to be entrained into and mixed with the fuel jet. The geometry of the kiln hood is quite intricate, with cross-sectional changes and bends, which, in combination with a large amount of process gas supplied asymmetrically, results in a complex flow field in the kiln. In addition, the backplate acts like a bluff body in the flow, with vortices shedding and a wake forming behind it. All of this has a significant impact on the fuel/air mixing and combustion process in general and the flame shape and stability, as well as the combustion efficiency, in particular.

A common saying is that there are three Ts necessary for good combustion: time, temperature, and turbulence. A sufficient residence time for reactions to occur, a required temperature to ignite the fuel mixture, and proper mixing (turbulence) between the fuel and oxygen. These three parameters govern the speed and completeness of the reactions and hence the combustion process [3].

The first step in the mixing process is kinematic, involving large-scale vortical structures entraining ambient fluid into the jet as they undergo pairing. Turbulent, and, finally, molecular diffusion then completes the mixing process at the smallest scales. The key step in the mixing process is the rate at which ambient fluid is entrained [4]. In reactive cases, the entrainment affects the residence time through the flame and the overall chemical reaction, so it is of fundamental interest to study the flow field dynamics and the entrainment process [5].

The heat flux characteristics of the diffusion flame (the length and luminosity) are dominated by the mixing process of the fuel, air, and combustion products. The emissions are also strongly influenced by the mixing field through their dependence on residence time at a given local temperature and mixture fraction [6].

Since the burner is in the back-end of the kiln, a long flame extending far into the kiln is wanted to benefit the pellet oxidation in the preheat (PH) zone in the grate, as well as the sintering process in the kiln. A luminous flame heats the bed mainly through radiative heat transfer, though conduction from the kiln walls also contributes to the heat transfer. The flame length is hence important, and a short flame can cause problems, with an uneven heat load to the pellet bed [7]. A controlled and predictable flame reduces the fuel amount needed and contributes to an increased process efficiency.

In order to achieve an optimal flame shape and heat flux profile with the most efficient combustion possible, the mixing rate of fuel and air needs to be controlled. One issue of reactive flows is that mixing and reactions interact with each other simultaneously, making the understanding of mixing more challenging. It is therefore desirable to study a mixing process with similar properties to a reactive flow, but without the effect of the reaction [8]. This can be carried out by using scaling parameters based on theories describing and defining the properties and mixing characteristics of an enclosed diffusion flame. The density variations in combusting systems are accounted for by distorting the nozzle diameter relative to the duct diameter (the kiln diameter in this case) or the nozzle flow in the isothermal, non-reactive model. This ensures that the momentum ratio of the co-flow relative to the jet in the model matches that of the reacting system [9,10]. The scaling parameter enables isothermal models of reactive flows to study the mixing process in detail.

The dynamics of the flow field in the iron ore rotary kiln, the kiln aerodynamics, has not been studied to any great extent in the literature. In general for rotary kilns, the focus has mainly been on the burner and how to improve the combustion process, both in terms of efficiency and environmental impact. However, the burner manufacturer is often separate from the kiln manufacturer, and the burner design is therefore given little consideration in terms of kiln aerodynamics. Hence, when installed, kiln burners often behave differently than expected due to the non-optimal flow field deviating far from the operating conditions assumed at design. This can lead to a very unstable flame that deviates from the kiln axis and causes damage to the product at the bottom or the kiln walls. A reduced combustion efficiency is another undesirable possible consequence [11].

There are several studies focusing on cement and lime kilns; Refs. [12–20] are some examples, showing the flow field dynamics effect on the mixing of fuel and air, flame properties and characteristics, and resulting emissions. There are similarities between the different industries; however, the geometry and the excessive secondary air flow in the iron ore kiln result in combustion conditions that are significantly different compared to other processes [2]. To optimize the combustion process, it is therefore necessary to have a good understanding of the kiln aerodynamics and the resulting mixing characteristics in the flow conditions of the iron ore rotary kiln.

The global pressure to control and reduce pollutant emissions and greenhouse gases has increased extensively over the last decades. Reducing or eliminating the use of fossil fuels in the pelletizing plant is necessary to obtain a sustainable iron value chain. The rotary kiln is one of the most difficult emission sources to abate, and LKAB is running several projects directed at reducing emissions from their pellet plants, including both primary and secondary measures. A summary can be found in [21].

One project is focusing on a systematic study of the iron ore rotary kiln aerodynamics and, by extension, its effect on the combustion process. The rationale behind the project is to control the flow field to optimize the mixing process of fuel and air and hence the evolution of the flame and its properties. By achieving this, it is possible to make the combustion process more efficient and reduce the amount of fuel used and, hence, the emissions, while maintaining or even increasing the quality of the pellets produced by creating an optimal temperature and gas profile throughout the kiln.

Since it is hard to perform measurements during operation due to the harsh environment with dust, high temperatures, and large mass flows of gas, simulation models can be a valuable tool for process understanding and control. Experimental validation is, however, a prerequisite for accurate numerical modeling; hence, systematic studies

of simplified and down-scaled geometries provide an efficient way of gradually moving forward toward valid models. This paper summarizes the results and highlights the main conclusions from over a decade of systematic studies of the kiln aerodynamics of an iron ore pelletizing rotary kiln involving computational fluid dynamics (CFD) modeling and validating experiments [11,22–31].

The paper is structured in four sections, where the working methodology is described in Section 2. The results are then synthesized and discussed in Section 3, and the conclusions, as well as planned future work, are presented in Section 4.

2. Methods

The approach of the project was to start as simple as possible using down-scaled, isothermal models to investigate the cold flow field without combustion. The commercial code Ansys CFX was used for the simulations. The code uses a coupled solver based on the finite volume method with a fully implicit discretization of the governing equations in every time step. The numerical results were validated against measurements in experimental models using different laser-based optical techniques, including particle image velocimetry (PIV), tomographic PIV, planar laser-induced fluorescence (PLIF), and laser doppler velocimetry (LDV).

Modeling reality requires certain assumptions and simplifications. It is important to identify the main physical parameters to be considered and those that can be omitted. Boundary conditions and input parameters affect all results, and the sensitivity of the CFD model must be carefully examined. The idea of the project was to gradually develop the model and validate the simulation results against experimental data before increasing the complexity and including more physics to better describe the reality. In a recent study, a coal combustion model was also applied in the simulations to allow for an investigation of the thermal effects of the flame on the surrounding flow field. These simulation results were partially compared to temperature measurements from the corresponding real pilot-scale kiln.

2.1. Geometries

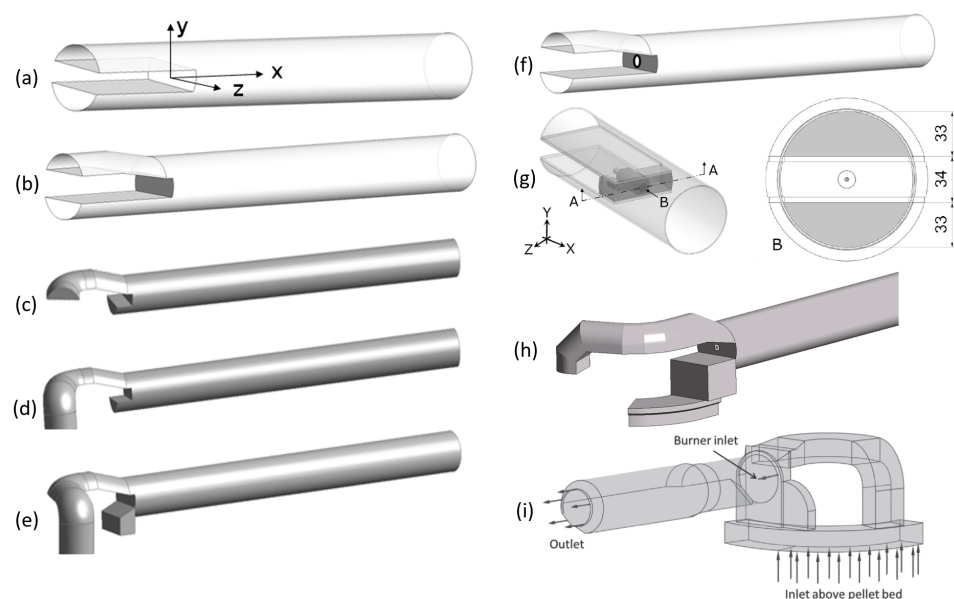Figure 3 shows the different geometries studied and the gradual shift toward more realistic models.

Figure 3. Geometries studied in the project: (**a**–**e**) only secondary flow, no burner jet and (**f**–**i**) burner jet included. (**f**) Single jet, (**g**) coaxial jets, (**h**) pilot-scale with coal combustion, (**i**) kiln with different type of hood, no backplate present. Figures adapted from [11,23–29].

The flow field and resulting mixing process were studied both without (Figure 3a–e) and with (Figure 3f–i) the burner jet included in the model, and the burner jet was modeled either as a single jet (Figure 3f) or coaxial jets (Figure 3g). Combustion was included in the model (Figure 3h), and another type of kiln with a different hood without the backplate was also studied (Figure 3i). The geometrical scale ranges from down-scaled lab models to pilot-scale.

2.2. Scaling Parameters

Reynolds number and the Craya–Curtet parameter were used to scale the geometries and the flows to account for isothermal conditions in the experimental models. The Craya–Curtet parameter was chosen as the most appropriate scaling parameter in this work when the burner jet is also included in the model [27]. It essentially corresponds to the momentum ratio of the jets (the nozzle flow and surrounding secondary co-flow) and is a measure of the dynamic mixing. It is always positive and varies between zero and infinity, and, depending on the value of the parameter, the flame has different characteristics. Short and intense flames have a higher Craya–Curtet parameter, whereas flames with a Craya–Curtet parameter between 1 and 2 are characterized as long flames. If the Craya–Curtet parameter is below 1, the flame tends to be long and lazy [32]. In this work, the Craya–Curtet parameter, calculated based on real kiln process parameters, is around 1, depending on the geometry (plant/real kiln) studied. The Reynolds number, Re, in the real full-size kiln is approximately 3.5×10^5, based on process parameters and kiln diameter. In the project, a reduced Re is often used due to the physical limitations of the experimental set-ups. This is not an issue though, since Re is still in the fully turbulent range, and reduced Reynolds similarity holds for turbulent jets [33].

2.3. Governing Equations and Turbulence Models

The Navier–Stokes equations are the governing equations for fluid flow, here stated for incompressible flow:

$$\frac{\partial v_i}{\partial x_i} = 0, \tag{1}$$

$$\frac{\partial v_i}{\partial t} + v_j \frac{\partial v_i}{\partial x_j} = -\frac{1}{\rho} \frac{\partial p}{\partial x_i} + \nu \frac{\partial^2 v_i}{\partial x_j^2}, \tag{2}$$

where v_i are the fluid velocity components, p is the fluid pressure, and $\nu = \mu/\rho$ is the kinematic viscosity.

Applying Reynolds decomposition, where a velocity component is divided into an average and a time-varying component ($v_i = \overline{v_i} + v_i'$) to the Navier–Stokes equations, the Reynolds averaged Navier–Stokes (RANS) equations are obtained:

$$\frac{\partial v_i}{\partial x_i} = 0, \tag{3}$$

$$\rho \frac{\partial \overline{v_i}}{\partial t} + \rho \overline{v_j} \frac{\partial \overline{v_i}}{\partial x_j} = -\frac{\partial \overline{p}}{\partial x_i} + \frac{\partial}{\partial x_j} (\overline{\tau_{ij}} - \rho \overline{v_i' v_j'}). \tag{4}$$

The equations are formally identical to the Navier–Stokes equations, with the exception of the additional term

$$\tau_{ij} = -\rho \overline{v_i' v_j'} = -\rho (\overline{v_i v_j} - \overline{v_i} \overline{v_j}), \tag{5}$$

which is the so-called Reynolds stress tensor. It represents the transfer of momentum due to turbulent fluctuations and acts as additional stresses in the fluid. The equations used to model the Reynolds stresses to close the system define the type of turbulence model.

Two-equation turbulence models are based on the eddy viscosity hypothesis of Boussinesq, where the Reynolds stresses are assumed to be linearly related to the mean velocity gradients, with the eddy viscosity, μ_t, as the proportionality constant

$$-\rho \overline{v_i' v_j'} = \mu_t \left(\frac{\partial \overline{v}_i}{\partial x_j} + \frac{\partial \overline{v}_j}{\partial x_i} \right) - \frac{2}{3} k \delta_{ij}, \tag{6}$$

where $k = \frac{1}{2} \overline{v_i' v_i'}$. One can also define the kinematic turbulent viscosity: $\nu_t = \mu_t / \rho$. The turbulent viscosity is isotropic, but not homogeneous.

Two dominant properties of the turbulence field are used to define an expression for the eddy viscosity: the turbulent kinetic energy, k, and its dissipation rate, ε, which determines the turbulent length scale. Through dimensional analysis, the following relationship is achieved:

$$\nu_t = C_\mu \frac{k^2}{\varepsilon}, \tag{7}$$

where C_μ is a model constant determined from experiments. Instead of using the dissipation rate, one can use a characteristic frequency of the turbulence decay process, according to $\omega = \varepsilon / k$. The relationship between the eddy viscosity and the eddy frequency is

$$\nu_t = C_\mu \frac{k}{\omega}. \tag{8}$$

Reynolds stress turbulence models do not use the isotropic eddy viscosity hypothesis; instead, individual transport equations for all components of the Reynolds stress tensor and the dissipation rate are solved.

Another turbulence modeling approach is to use large eddy simulation (LES), where the large-scale structures are resolved, whereas the smaller scales are modeled. This is achieved through a spatial filtering operation applied to the Navier–Stokes equations. The resulting filtered equations look similar to the RANS equations. It should, however, be noted that, while the Reynolds stress tensor in the RANS equations includes all turbulent effects in the momentum equation, the corresponding subgrid-scale stress tensor in the LES filtered equations only includes turbulent effects smaller than those that the grid can resolve.

The turbulence models used in this work include the two-equation models $k - \varepsilon$ and shear stress transport (SST) [34], the Reynolds stress baseline model (RSM-BSL) based on the baseline ω-model by Menter [35], and the detached eddy simulation model (DES), a hybrid RANS/LES model originally proposed by Spalart [36]. In the DES model, the large scales are resolved by LES, whereas the smaller scales are modeled using SST [37]. The DES model switches from SST to LES in regions where the turbulent length scale predicted by the RANS model is larger than the local grid spacing; hence, great care must be taken when generating the grid. The RANS model is used in both regions; in the LES region as subgrid-scale model. In the RSM-BSL model, the ω-formulation is applied as the scale determining equation, whereas the SST model is based on the hybrid $k - \varepsilon / k - \omega$ formulation, where $k - \omega$ is used near the walls and the $k - \varepsilon$ formulation is recovered in the bulk flow. SST is useful in flows with an adverse pressure gradient or in separating flows. The Reynolds stress model BSL solves six additional equations for the Reynolds stresses, with one equation for the dissipation (in an ω-formulation) of the flow, and is suitable for more complex flows, such as swirling, and secondary flows where the isotropic eddy viscosity assumption is no longer valid. The disadvantage of the model is a decrease in the numerical stability and an increased computational cost compared to a two-equation model [38].

When studying the simpler geometries, ω-based turbulence models were used since the advantage of the ω-formulation in the near wall treatment makes it easier to avoid wall functions and resolve the boundary layer, given that the grid requirements are met ($y^+ < 2$ and 10–15 nodes in the boundary layer). The code used favors the ω formulation in the near wall treatment. Resolving the boundary layer is especially important when modeling

secondary flows: the flow in the transverse plane perpendicular to the mean axial flow that develops in ducts with bends and/or non-circular cross-section, such as the secondary air ducts to the kiln.

2.4. Boundary Conditions

To quantify the distribution of mass flow between the ducts, the momentum flow ratio, M_{sec}, based on the flow through each separate secondary inlet, is used in the project. The momentum flow in each secondary inlet is approximated with the mass flow squared, $\dot{m}_1$, for the upper inlet and $\dot{m}_2$ for the lower inlet, meaning that the momentum flow ratio $M_{sec} \approx (\dot{m}_1/\dot{m}_2)^2$. This is a simplification, but the only purpose is to conveniently describe the different mass flow distributions between the secondary fluid inlets. A momentum flow ratio of one corresponds to a matched mass flow between the inlets, and increasing the ratio means that the mass flow distribution becomes uneven with a dominating upper flow if not explicitly stated otherwise. When the burner jet is included in the model, the momentum flow ratio of the coaxial outer to inner jet is defined as $M_{jet} = (\rho_o U_o^2 A_o)/(\rho_i U_i^2 A_i)$. $M_{jet} = 0$ corresponds to a single jet. The momentum flow ratios M_{sec} and M_{jet} are varied to evaluate the effect on the flow field and the resulting mixing process between the different flow streams.

In the CFD simulations, mass flow plug profiles with a turbulence intensity of 5% were used as inlet boundary conditions. An average static pressure was employed at the outlet with a relative pressure of zero Pa, averaged over the whole outlet. The walls were smooth with no slip. The discretization schemes include a formally second-order accurate scheme for the advection term (upwind) and the transient term (backward Euler) for the unsteady cases. The turbulence equations were discretized using a scheme that blends between first and second-order accurate upwind schemes. When LES was applied, the advection term was discretized using a central differencing scheme. A converged steady-state solution initialized the transient simulations, and a non-dimensionalized time step of $tU_b/D = 0.01$ (where U_b is the bulk velocity in the kiln and D the kiln diameter) was used in the transient simulations.

Grid studies were conducted in all numerical work. Between 3–5 grids were used and both local and global values of dependent, key variables were investigated to estimate the grid dependence and the discretization error. The difference between the two finest grids varied between approximately 1–2.7% depending on the parameter and case studied. Great effort was spent on generating high-quality grids to reduce the discretization error.

The working fluid was water in all studies except the coal combustion simulations. Water allows a smaller scale of the model kiln with lower flow velocities, facilitating the experimental work, as previously mentioned.

Table 1 shows an overview of the cases studied in this project. For full details about all studies summarized in this paper, including modeling assumptions, boundary conditions, and numerical and experimental set-ups, the interested reader is referred to the cited sources in the table below and in the following sections.

Table 1. Boundary conditions.

Geometry [ref]	Method	Mesh	Turbulence Model	Flow Rates Secondary Inlets (Total)	Burner Jet	Mom. Ratio	Other Information
Figure 3a [23]	CFD, PIV	12.5 M nodes, hexahedral	RSM-BSL	3.95 kg/s, 7.9 kg/s	N/A	$M_{sec} = 1, 2.27, 5.44$	Steady state, isothermal, no wall func.
Figure 3b [24,25]	CFD, PIV	18 M nodes, hexahedral	SST, RSM-BSL, DES	7.9 kg/s	N/A	$M_{sec} = 1, 2.27, 5.44$	Transient, isothermal, no wall func.
Figure 3c–e [26]	CFD	3 M nodes, hexahedral	RSM-BSL	7.9 kg/s	N/A	$M_{sec} = 1$	Transient, isothermal, wall func.
Figure 3f [27]	PIV, PLIF	N/A	N/A	2.16 kg/s	0.0315 kg/s	$M_{sec} = 1, 2.26, 5.44$	Single jet, isothermal
Figure 3g [28]	PIV, PLIF	N/A	N/A	0.78 kg/s	Inner coaxial: 0.0133 kg/s; Outer coaxial: 0, 0.0138, 0.0197, 0.0382 kg/s	$M_{sec} = 1, 5.44; M_{jet} = 0, 0.5, 1, 3.8;$	Coaxial jets, isothermal
Figure 3h [11]	CFD	1.5 M nodes, tetra and prism	$k - \varepsilon$	2914 kg/h	13 kg/h gas, 70 kg/h pulverized coal	$M_{sec} = 2.27$	Steady state, coal comb., thermal, wall func.
Figure 3i [29]	CFD	1 M nodes, tetra and prism	$k - \varepsilon$, RSM-BSL	38.3665 kg/s	0.0374 kg/s	N/A	Transient, isothermal, wall func.

3. Results and Discussion

The flow field in the kiln is quite complex since it is highly turbulent and unsteady. Several fluid mechanical phenomena are occurring, such as jet entrainment and recirculation, in different areas throughout the kiln, both internal and external. Due to the confinement and the velocity gradients between the different inlet streams, there are several shear layers arising in the flow, some of them involving Kelvin–Helmholtz instabilities. There is vortex shedding occurring behind the backplate and secondary flow arising in the transversal plane perpendicular to the mean axial flow due to the geometry, which is most likely a combination of turbulent and pressure-driven secondary flow since the air ducts have bends and non-circular cross-sections [26].

The results focus on five main aspects and their effect on the mixing process and the flow field dynamics:

- Mass flow distribution between the secondary inlets;
- Geometry of the kiln hood;
- Inclusion of the burner jet;
- Heat release from the flame;
- Choice of turbulence model.

The key findings from the different studies are highlighted and elaborated on in the following subsections. The results of this project will also be put into a broader context when the latest research advances in rotary kilns for mineral processing, and, in particular, rotary kilns for iron ore pelletization, will be discussed at the end of this section.

3.1. Vortex Shedding

The vortex-shedding process results in large-scale oscillations and involves the most energy-containing motions of the flow in the kiln [24,26]. Figure 4 shows the vorticity field in the vertical center plane of the two simplest geometries without the burner jet (for reference, see Figure 3a,b). Only the secondary fluid is modeled, and no burner jet is present.
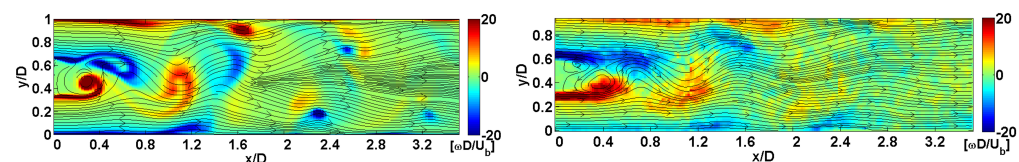

Figure 4. Vortex shedding behind the backplate, spanwise vorticity in the vertical symmetry plane with velocity streamlines (for geometry, see Figure 3a,b). CFD results to the left and PIV results to the right. Figure adapted from [39].

The shedding process highly depends on the mass flow distribution between the secondary flow inlets. The largest oscillations of the flow field are seen when the mass flow is evenly distributed, where $M_{sec} = 1$. When one jet becomes dominant, the weaker jet is entrained into the dominant one and the flow field is stabilized. The dominant frequency of the vortex shedding in the simpler geometries is approximately 12 Hz, corresponding to a Strouhal number of approximately 0.17 based on the height of the backplate. The vortex shedding and the resulting large-scale oscillations in the flow means that the two secondary jets are mixing faster when $M_{sec} = 1$ [24]. The important aspect in this project, however, is how the fuel jet from the burner is mixed with the secondary flow; this will be discussed in a subsequent paragraph.

3.2. Recirculation Zone

An area of particular interest is the recirculation zone that develops in the wake behind the backplate. From a combustion perspective, this region is important since the reversed flow improves the flame stability and affects the combustion efficiency. Since the flow field

is strongly affected by the geometry and the mass flow distribution between the inlets, the appearance and length of the recirculation zone also depend on these parameters; see Figure 5. In the simpler models with almost parallel secondary flow jets, the recirculation zone in the wake behind the backplate is clearly seen. A completely different flow field is seen when the geometry is developed towards a more realistic model. The jets are no longer parallel, which has a great impact on the resulting flow field. Due to the geometry, two main low-velocity regions develop, one behind the backplate and one below the jet emerging from the lower inlet, resulting in several areas with recirculating fluid [26].
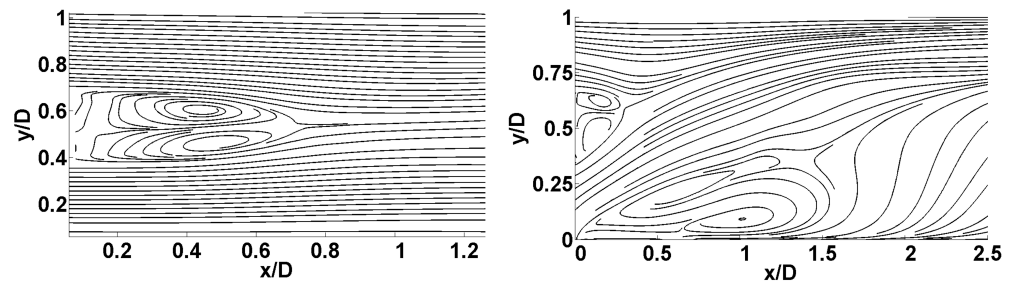

Figure 5. Recirculation zones in the vertical symmetry plane in the kiln, with PIV results to the left (for geometry, see Figure 3b) and CFD results to the right (for geometry, see Figure 3e). Figure adapted from [39].

3.3. Burner Jet

When introducing the burner jet in the model and studying only a single jet emanating from the middle of the backplate, it is seen that the burner jet characteristics, as well as the flow field surrounding the jet, are affected by the mass flow distribution between the secondary flow inlets [27,28]. Figure 6 shows an overview of the flow field illustrating the entrainment of the secondary flow into the burner jet. Again, varying the mass flow distribution between the secondary inlets results in different external recirculation zones occurring around the jet. For a combusting case, a reasonable amount of external recirculation shows that the fuel/air mixing is complete, whereas the absence of recirculation indicates that not all necessary secondary air has been entrained, leading to incomplete combustion with increased emissions. A lack of external recirculation in a confined flame can also lead to excessive expansion of the flame, which destroys the product and the refractory walls [9].
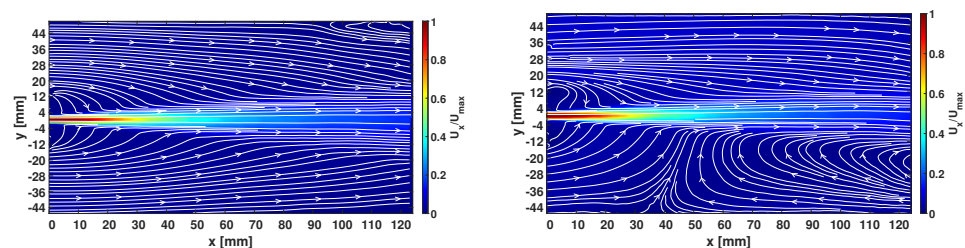

Figure 6. Mean flow field in the vertical symmetry plane with a single burner jet included in the model (for geometry, see Figure 3g), with $M_{sec} = 1$ to the left and $M_{sec} = 5$ to the right. The contours show the burner jet axial velocity and the streamlines show the entrainment of the secondary flow into the jet. Figure adapted from [28].

As previously mentioned, the vortex-shedding process and the resulting large-scale oscillation of the flow field in the kiln increase the mixing of the secondary jets. The opposite trend is indicated when the burner jet is incorporated and its mixing with the secondary flow is scrutinized. The shedding process breaks up the burner jet on a large scale (see Figure 7) but the mixing between the burner fluid and the secondary fluid, which takes place on a small scale, seems to be promoted by a continuous shear layer, which results from

an uneven mass flow distribution of the secondary flow [27]. It is clear from the experiments that the secondary flow considerably affects the burner jet and the mixing characteristics.
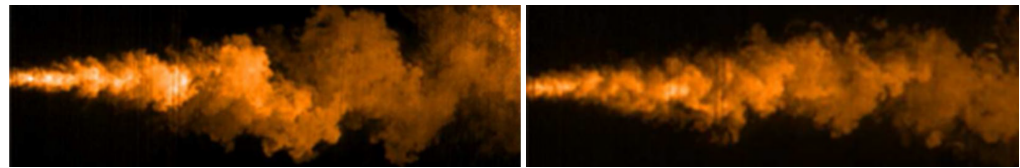

Figure 7. Instantaneous PLIF images of the burner jet in the vertical symmetry plane (for geometry, see Figure 3f), with $M_{sec} = 1$ to the left and $M_{sec} = 5$ to the right. Figure adapted from [27]. Reprinted with permission from Springer Nature.

How the introduction of a coaxial outer stream affects the mixing process of the burner jet and the secondary, co-flowing fluid has also been studied experimentally [28]. The main objective was to investigate the possibility of controlling the burner jet length. How varying the velocity ratio between the inner and outer stream affects the jet development, as well as the effects of varying the mass flow ratio between the upper and lower secondary flow inlets, were both investigated. The results show that it is possible to affect the mixing of the central jet and the secondary fluid and, hence, affect the jet length by introducing a coaxial stream. The outer coaxial stream shields the inner burner jet, decreasing the mixing with the secondary, co-flowing fluid. Figure 8 shows probability density functions (PDF:s) of the concentration in five points along the centerline, illustrating the mixing process. High and narrow distributions indicate that the concentration does not vary much over time, and low and wide distributions indicate that mixing is taking place. Note that the appearance of the PDF:s of $M_{jet} = 3.8$ (Figure 8d) shows the closest resemblance to $M_{jet} = 0$ (Figure 8a). The low and wide distributions for $M_{jet} = 3.8$, however, implies good mixing between the inner and outer stream of the coaxial jets, but not with the secondary flow in the wake, which is the case for $M_{jet} = 0$. It was also clear from the experiments that the secondary flow distribution affects the shape and direction of the central jet.
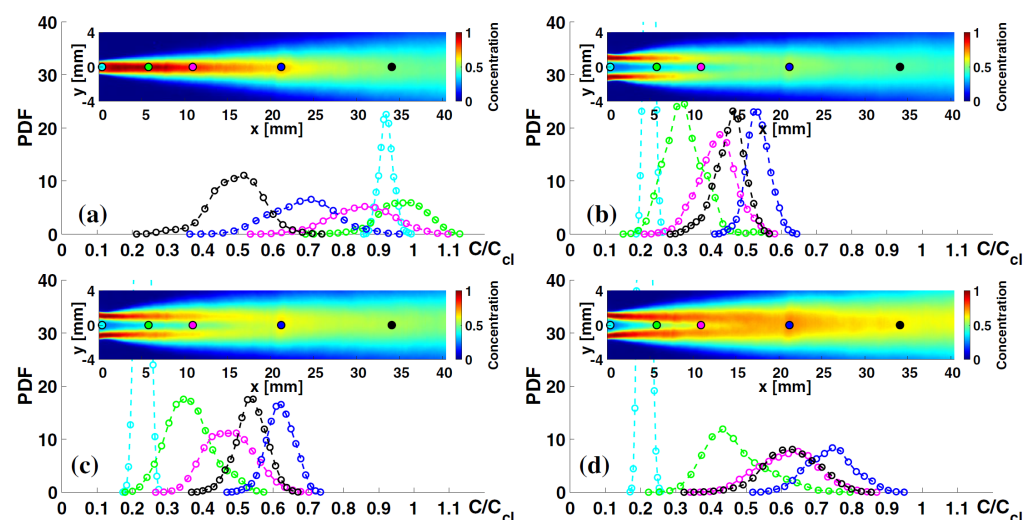

Figure 8. Probability density functions along the centerline (for geometry, see Figure 3g). $M_{sec} = 1$ for all cases. (**a**) $M_{jet} = 0$, (**b**) $M_{jet} = 0.5$, (**c**) $M_{jet} = 1$, (**d**) $M_{jet} = 3.8$. Figure adapted from [28].

3.4. Coal Combustion Modeling

In the most recent work of the project, a basic coal combustion model was included in the simulations to investigate how the combustion process affects the flow field [29]. The pulverized coal was treated as Lagrangian particles undergoing devolatilization and char oxidation, with gas-phase combustion of the released volatiles modeled using a single

step eddy viscosity model. The discrete transfer model was applied to account for thermal radiation. For details of the coal combustion modeling, see [29] and references therein.

Hot gas flow without and with combustion present was modeled in pilot-scale and it was found that the combustion process with the resulting temperature rise and volume expansion leads to an increase in the velocity in the kiln. The temperature rise is seen throughout the kiln, but it is largest close to the flame, where the temperature is highest. Apart from the velocity increase, the flow field looks similar whether or not combustion takes place.

Figure 9 shows the evolution of the velocity in the transversal plane downstream the kiln; also, here, it is obvious that no significant differences, apart from the velocity magnitude, can be seen between the hot gas flow and the combustion case. The flow develops similarly and the vortices occur in more or less the same places for both cases. After the ignition of the flame and the start of the combustion process, the average velocity in the transversal plane increases by about 30% for the combustion case compared to the hot gas flow.
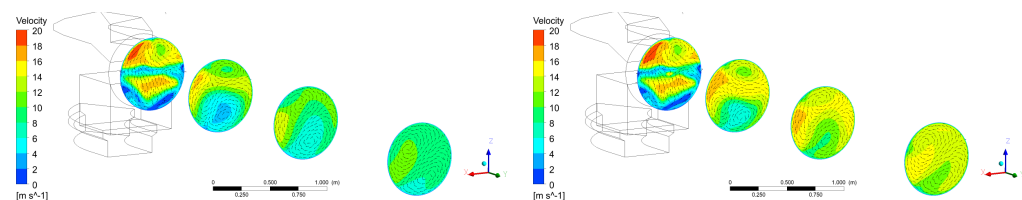

Figure 9. Velocity contours with tangentially projected velocity vectors at four transversal planes downstream the kiln, with hot gas flow to the left and combustion to the right. Figure adapted from [29].

Looking closer at the influence of the combustion process on the secondary flow streams—see Figure 10—it is revealed that no substantial distortion occurs in the vertical center plane. The merging streams are, however, closer to the centerline when combustion is present compared to when it is not, leading to a suppression of the recirculation zone that develops in the lower part of the kiln (Figure 10a,b). This is also clearly visible when looking at the horizontal center plane, which also shows that the flow is pushed toward the left side of the kiln (Figure 10c,d).
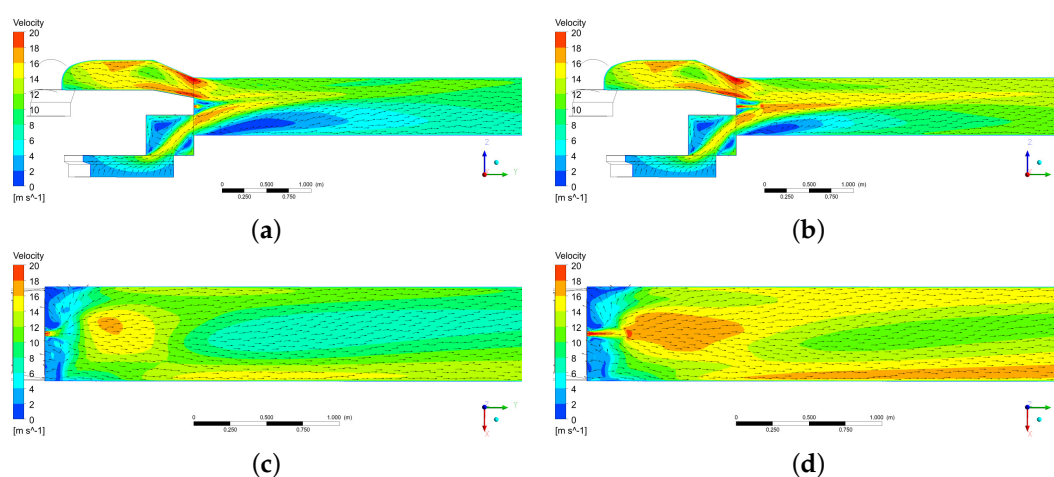

Figure 10. Velocity vectors tangentially projected on the vertical center plane on top, and the horizontal center plane below. (**a**) Hot gas flow vertical center plane. (**b**) Combustion vertical center plane. (**c**) Hot gas flow horizontal center plane. (**d**) Combustion horizontal center plane. Figure adapted from [29].

The general conclusion from this study is that the overall flow field in this kiln is not significantly affected by the heat release and gas volume expansion due to the flame.

The flow field, however, governs the flame propagation and influences the combustion process by controlling the mixing rates of fuel and air. A comparison of the simulation results to the measurements in the real pilot-scale kiln was also carried out. A point measurement in the kiln outlet under similar operating conditions showing a temperature of 1320 °C agrees well with the simulated kiln outlet temperature, which varies between 1318 and 1411 °C over the area, with an average value of 1393 °C.

3.5. Kiln Hood without Backplate

Another type of kiln used by LKAB was also simulated, where the hood geometry differs from the main geometry studied in this work; see Figure 3i [11]. There is no backplate; instead, the burner is mounted like a lance, extending about one-third of the kiln diameter into the kiln. In addition, part of the annular cooler is modeled to achieve realistic inflow conditions for the kiln. The objective of the study was to evaluate the possibility of predicting the flame shape through an isothermal CFD simulation of a down-scaled, simplified model. The mixing process of the jet fluid and the surrounding flow was investigated by solving a transport equation for a passive scalar defined as the burner jet fluid. The simulation results were compared to recorded images of the flame during operation in the real, full-scale kiln.

The results were promising, with the isothermal simulations capturing the main, unsteady behavior of the flame seen in the real process; see Figure 11.
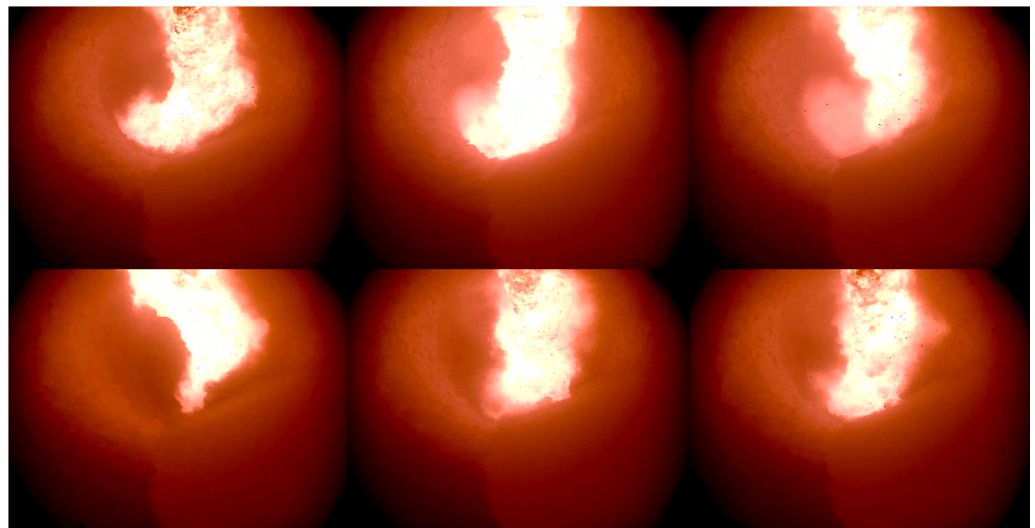

Figure 11. Images recorded in the real process showing the unsteady flame. Figure adapted from [11]. Reprinted with permission from the Society for Mining, Metallurgy & Exploration.

By plotting isosurfaces of a vortex identification parameter, it is possible to reveal the flow structures. From Figure 12, it is seen that the unsteadiness evolves from the design of the kiln hood. The ducting and the kiln hood geometry lead to the evolution of several vortices in the area around the burner nozzle, which have a great impact on both the resulting flow field in the kiln and the burner jet flow; see Figures 12 and 13.
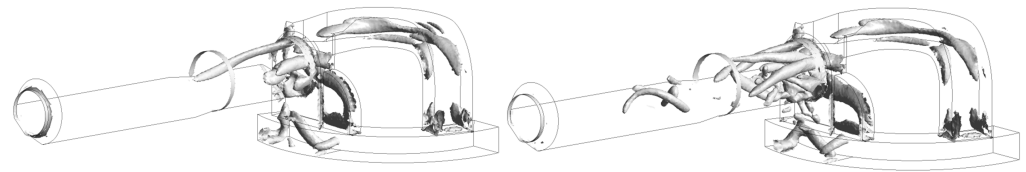
Figure 12. Visualization of vortices by isosurfaces of the vortex identification parameter, the Q-criterion. Results from the two-equation turbulence model $k - \varepsilon$ to the left and the Reynolds stress model RSM-BSL to the right. Figure adapted from [11]. Reprinted with permission from the Society for Mining, Metallurgy & Exploration.

Figure 13. Time-averaged streamlines in the kiln, where the black streamlines show the predicted trajectory of the burner jet. Results from the two-equation turbulence model, with $k - \varepsilon$ to the left and the Reynolds stress model RSM-BSL to the right. Figure adapted from [11]. Reprinted with permission from the Society for Mining, Metallurgy & Exploration.
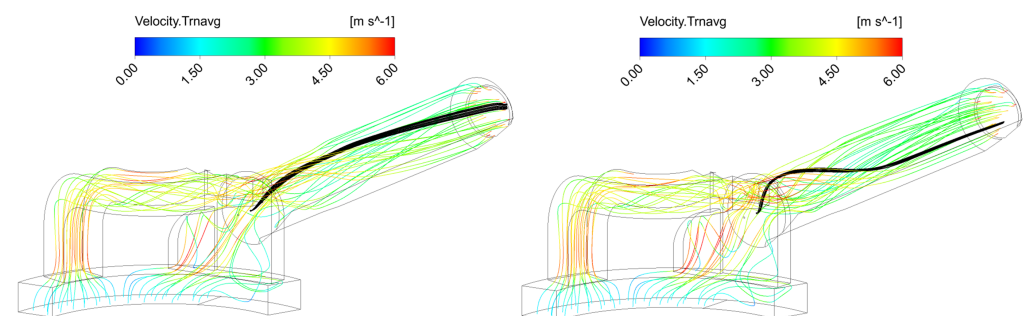
Since the combustion is neglected, the volumetric expansion of the flame is missed, along with temperature and density variations in the domain. This might change the secondary air entrainment and the resulting mixing of fuel and air, which affects the burner jet flame characteristics [9]. However, as seen in the combustion simulations of the pilot-scale kiln described earlier, the heat release and the resulting gas volume expansion due to the flame do not significantly affect the overall flow field. The flow field, however, governs the flame propagation and influences the combustion process by controlling the mixing rates of fuel and air. The results show the importance of taking the fluid mechanics in general, and the kiln aerodynamics in particular, into consideration when designing the burner to achieve optimal operating conditions of the kiln.

3.6. Turbulence Modeling

The simulation results of this project show that the turbulence models produce quite different results, yielding various predictions of the flow field in the kiln [25]. Specifically, the two-equation model SST cannot capture the unsteady flow with large-scale instabilities that the geometry gives rise to behind the backplate. One probable reason for this is the well-known deficiency of two-equation models, with over-prediction of the turbulent kinetic energy in regions with strong acceleration or deceleration, where too much kinetic energy results in a high level of eddy viscosity that damps the vortex shedding. Simulations on the simpler geometries also showed that the DES model is computationally demanding and performed poorly on the grid applied. As stated earlier, careful grid generation is required. The Reynolds stress model (RSM-BSL) showed good results when validated against experiments; see Figure 14. The model can show secondary flow, both turbulence and pressure-driven ones, and gives a good overview of the most energy-containing motions of the flow field without being too computationally expensive. How well the turbulence model can predict the incoming flow from the secondary inlet ducts strongly affects the evolution of the flow field in the kiln. This was clearly observed in the simulation work.
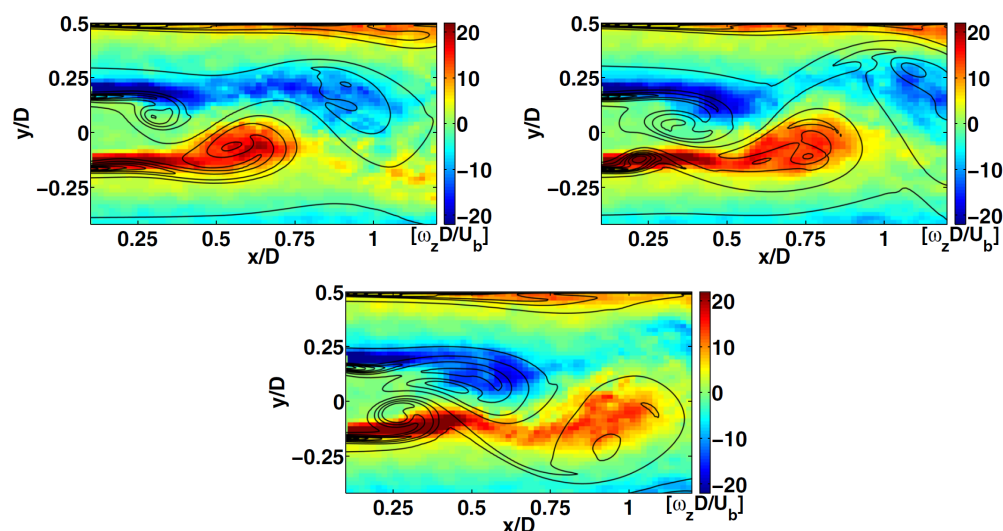
Figure 14. Snapshots from the vortex-shedding cycle showing spanwise vorticity in the vertical symmetry plane (for geometry, see Figure 3b). Comparison between simulations using the RSM-BSL model (black contours) and PIV experiments (colored contours). Figure adapted from [25]. Reprinted with permission from Springer Nature.

When the model was developed towards a more realistic geometry with more physics (including the burner jet and, in one case, also coal combustion), wall functions were used with both the RSM-BSL and the $k - \varepsilon$ turbulence models, since it was too computationally expensive to resolve the boundary layers. The $k - \varepsilon$ turbulence model is commonly used when modeling coal combustion in large-scale industrial furnaces, and it is one of the most widely used turbulence models due to its robustness and ability to solve a wide range of flow fields without being too computationally expensive. The results, however, revealed that the model could not capture the unsteady flow field and the swirling motion of the "flame" (burner jet) as well as the Reynolds stress model did; see Figures 12 and 13. The isotropic Boussinesq assumption that two-equation models are based on leads to poor predictions of three-dimensional effects in flows with strong separation and in fully developed turbulent flow in non-circular ducts; this profoundly affects the resulting flow field in the kiln, given the geometries studied in this work.

In general, the simulation results show that moving from a RANS formulation to an eddy-resolving method such as DES does not necessarily yield improved or correct predictions. Realistic inflow conditions, as well as grid-dependence and sensitivity studies combined with validating experiments, are necessary to generate confidence in the results. This justifies the strategy of the overall project with a gradually increasing complexity of the model in the pursuit of a validated full-scale simulation model of the iron ore pelletizing rotary kiln that can be used for process optimization.

3.7. Latest Research Advances in Rotary Kilns for Mineral Processing

Rotary kilns are used to process a variety of materials, the most common of which are cement and lime, which naturally leads to the bulk of the literature being focused on these processes, as described in the introduction. To put the results presented in this paper in a broader context, some of the latest research regarding rotary kilns will be discussed, with a focus on iron ore pelletizing rotary kilns. The common denominator of all research on rotary kilns is that process optimization in terms of the yield, energy consumption, and pollutant emissions is the main objective. Due to the complexity of the process, it is difficult to obtain a complete picture of all influencing factors, and, therefore, limited and well-defined parts of the process are studied in detail.

Edland et al. [2,21,40] have performed several numerical and experimental studies focusing on combustion efficiency and NOx formation in iron ore pelletizing rotary kilns.

They found that the main contributor to NOx formation is the fuel-bound nitrogen, and that the char combustion plays a significant role. Their results also showed that the choice of the combustion process scaling parameter between pilot and full-scale is important, and that the constant velocity scaling criteria commonly used provide an accurate scaling of combustion settings and velocity and temperature profiles, but not the oxygen concentration experienced by the fuel during char combustion. It is critical to be aware of the differences induced by the scaling parameter since it has a major effect on the evaluation of appropriate NOx abatement measures. They suggest two approaches to mitigate NOx emissions: increasing the pyrolysis temperature to deplete the char of nitrogen or switching to a fuel with a lower nitrogen content, which are both primary measures, because the large volume of flue gas from the process makes secondary measures difficult and expensive. They also underline the importance of taking the pelletizing process into account when modifying the combustion process, since the sintering of pellets requires a controlled heat and gas profile to generate a high-quality product.

The heat transfer in an iron ore rotary kiln, both with and without a bed of pellets present, was modeled in full-scale and three dimensions by Gunnarsson et al. [41,42] using a discrete ordinates method. The results showed that 80% of the total heat transfer to the bed originates from radiation (whereas the rest is a result of conduction and convection), implying the importance of the accurate modeling of the radiative heat transfer to predict the total heat transfer in the kiln. The model can be used as a submodel in a more comprehensive combustion model.

Combustion using renewable fuels has been investigated experimentally by Wiinikka et al. [43] and Koveria et al. [44], where the latter study found that partially replacing natural gas with biomass consisting of crushed sunflower husks generated enough heat to obtain iron ore pellets with good strength. The results from Wiinikka et al. [43] showed that it is challenging to entirely replace coal with biomass since the temperature profile will be altered. A reduced oxygen content in the flue gas was also measured and the effect of these two factors on the pellet quality needs to be further investigated. There is also a risk for increased ash-related operational problems with biomass. Wang et al. [45] reviews the deposit formation in coal-fired iron ore pelletizing rotary kilns, describing the mechanisms to shed light on how to implement measures to prevent it in order to ensure the efficient production of pellets.

Relevant studies of cement kilns recently published include the work of Nial et al. [13], Lahaye et al. [19], and el Abbassi et al. [20]. All studies involve CFD simulation models of combustion and fluid flow, and the aerodynamics of the kiln and how to utilize it to optimize the flame and the resulting combustion process is in focus. It is found that the distribution of the secondary air around the burner strongly affects the NOx formation, and that a kiln hood geometry enabling a co-axial secondary air inlet promotes a lower thermal NOx formation due to a more evenly spatially distributed heat release with lower peak temperatures [19]. The results also show that two-dimensional models can provide acceptable information regarding the thermal behavior, while accurate flow field prediction requires a full three-dimensional model [19,20]. The central recirculation zone is important from a flame stability perspective and, regarding the turbulence modeling, it is suggested that the Reynolds stress baseline model (RSM-BSL) provides a good trade-off between computational effort and flow details [13].

Although several of the studies mentioned here report results showing the importance of the flow field, there are no detailed, systematic studies of kiln aerodynamics, apart from the author's own work, published in the literature.

4. Conclusions

Despite all of the simplifications regarding the models studied in this project, the results show the importance of correctly predicting the flow field in this type of kiln, where there is a large amount of process gas circulating, in order to optimize the mixing and combustion process. Since the combustion simulations revealed that the heat release does

not affect or change the flow field in any significant way, the use of down-scaled water models for investigating kiln aerodynamics in general and mixing properties in particular is justified. Although the heat release from the flame cannot be accounted for in isothermal models, important information regarding the real process is still gained. However, to better model the actual process numerically, more advanced submodels for both the combustion and especially the flow field are needed. The work shows that the complex flow field in this type of rotary kiln requires a careful choice of turbulence model to obtain accurate simulation results.

In terms of environmental impact, there is much to be gained by improving the current pelletizing process to reduce the carbon footprint and NOx emissions. The next major step in the near future is to replace the fossil fuels, coal and oil, in LKAB's current processing plants. Hydrogen is a likely fuel alternative as it can be produced on-site using electrolysis without carbon dioxide emissions. However, it is not possible to directly replace the fossil fuels with hydrogen in LKAB's current rotary kilns [43].

As described in the introduction, the grate–kiln process depends on the burner producing a long flame that generates heat throughout the whole kiln and to the earlier stages of the process. In today's coal flame, the slow reaction rates of the char, together with the high inlet momentum of the solid fuel flow, are strong contributors to the flame length. In a hydrogen flame, the flame properties will be dictated by the mixing of fuel and oxygen and, to create a long flame, high inlet velocities must be combined with slow mixing between the fuel and oxidizer. The task is complicated by the large amounts of hot process gas supplied through the kiln hood.

Hence, changing the fuel completely alters the operating conditions, which will affect the heat release and the temperature profile, which directly impact the pellet quality. A key factor, therefore, is to understand how to fluid mechanically design the optimal thermal and gas composition profile in the process to achieve the desired pellet quality regardless of the fuel used.

One idea that has been initially studied (and shortly described in this paper) and will be further explored is to introduce a coaxial flow stream surrounding the high-velocity fuel jet in order to decrease the mixing rate to the degree needed to create the thermal and gas composition profile desired for a high pellet quality. By fluid mechanically controlling the resulting shear layers, the mixing of fuel and oxygen may be regulated, giving a possibility to optimize the combustion process and flame properties. One unwanted side effect of hydrogen combustion in the presence of air to be aware of, however, is the possibility of generating thermal NO if the temperature gets sufficiently high [46].

Future work, therefore, includes investigating the feasibility of replacing solid fossil fuels with gaseous hydrogen in the iron ore pelletizing rotary kiln. The main challenges from a momentum, heat, and mass transfer perspective will be identified. Determining the flame length achievable for a 100% gas-fired flame in the flow conditions of LKAB's rotary kiln is the first step on the way.

Conflicts of Interest: The author declares no conflict of interest.

References

1. Stjernberg, J.; Isaksson, O.; Ion, J. The grate-kiln induration machine—History, advantages, and drawbacks, and outline for the future. *J. S. Afr. Inst. Min. Metall.* **2015**, *115*, 137–144. [CrossRef]
2. Edland, R.; Normann, F.; Fredriksson, C.; Andersson, K. Implications of Fuel Choice and Burner Settings for Combustion Efficiency and NOx Formation in PF-Fired Iron Ore Rotary Kilns. *Energy Fuels* **2017**, *31*, 3253–3261. [CrossRef]

3.　Doost, A.; Ries, F.; Becker, L.; Bürkle, S.; Wagner, S.; Ebert, V.; Dreizler, A.; di Mare, F.; Sadiki, A.; Janicka, J. Residence time calculations for complex swirling flow in a combustion chamber using large-eddy simulations. *Chem. Eng. Sci.* **2016**, *156*, 97–114. [CrossRef]

4.　Sreenivas, K.R.; Prasad, A.K. Vortex-dynamics model for entrainment in jets and plumes. *Phys. Fluids* **2000**, *12*, 2101–2107. [CrossRef]

5.　Han, D.; Mungal, M. Direct measurement of entrainment in reacting/nonreacting turbulent jets. *Combust. Flame* **2001**, *124*, 370–386. [CrossRef]

6.　Nathan, G.J.; Luxton, R.E. A Low NOx Gas Burner with a Radiant Flame. In *Energy Efficiency in Process Technology*; Pilavachi, P.A., Ed.; Springer: Dordrecht, The Netherlands, 1993; pp. 883–892. [CrossRef]

7.　Bäckström, D.; Johansson, R.; Andersson, K.; Wiinikka, H.; Fredriksson, C. On the use of alternative fuels in rotary kiln burners—An experimental and modelling study of the effect on the radiative heat transfer conditions. *Fuel Process. Technol.* **2015**, *138*, 210–220. [CrossRef]

8.　Li, W.; Yuan, M.; Carter, C.D.; Tong, C. Experimental investigation of the effects of mean shear and scalar initial length scale on three-scalar mixing in turbulent coaxial jets. *J. Fluid Mech.* **2017**, *817*, 183–216. [CrossRef]

9.　Mullinger, P.; Jenkins, B. *Industrial and Process Furnaces: Principles, Design and Operation*, 1st ed.; Butterworth-Heinemann: Oxford, UK, 2008. [CrossRef]

10.　Parham, J.J.; Nathan, G.J.; Hill, S.J.; Mullinger, P.J. A modified Thring-Newby scaling criterion for confined, rapidly spreading, and unsteady jets. *Combust. Sci. Technol.* **2005**, *177*, 1421–1447. [CrossRef]

11.　Larsson, I.A.S.; Lundström, T.S.; Marjavaara, B.D. Simulation of the flow field in an iron ore pelletizing kiln. *Miner. Metall. Process.* **2016**, *33*, 144–148. [CrossRef]

12.　Elattar, H.F.; Specht, E.; Fouda, A.; Bin-Mahfouz, A.S. Study of Parameters Influencing Fluid Flow and Wall Hot Spots in Rotary Kilns using CFD. *Can. J. Chem. Eng.* **2016**, *94*, 355–367. [CrossRef]

13.　Nial, M.; Loukarfi, L.; Naji, H. Aerodynamic control of a diffusion flame to optimize materials' transition in a rotary cement kiln. *Mech. Ind.* **2020**, *21*, 414. [CrossRef]

14.　Koptsev, V. Modeling the aerodynamics of the burners in kilns. *Metallurgist* **2004**, *48*, 548–552. [CrossRef]

15.　Elattar, H.; Stanev, R.; Specht, E.; Fouda, A. CFD simulation of confined non-premixed jet flames in rotary kilns for gaseous fuels. *Comput. Fluids* **2014**, *102*, 62–73. [CrossRef]

16.　Ma, A.c.; Zhou, J.m.; Ou, J.p.; Li, W.x. CFD prediction of physical field for multi-air channel pulverized coal burner in rotary kiln. *J. Cent. South Univ. Technol.* **2006**, *13*, 75–79. [CrossRef]

17.　Mikulčić, H.; Cerinski, D.; Baleta, J.; Wang, X. Improving Pulverized Coal and Biomass Co-Combustion in a Cement Rotary Kiln by Computational Fluid Dynamics. *Chem. Eng. Technol.* **2019**, *42*, 2539–2545. [CrossRef]

18.　Favalli, R.; Fabiani, L.; Pinho, L. Enhancing the performance of kiln burners. *World Cem.* **2015**, *43*, 111–114.

19.　el Abbassi, M.; Lahaye, D.; Vuik, C. The Effect of Variable Air–Fuel Ratio on Thermal NOx Emissions and Numerical Flow Stability in Rotary Kilns Using Non-Premixed Combustion. *Processes* **2021**, *9*, 1723. [CrossRef]

20.　Lahaye, D.; Abbassi, M.e.; Vuik, K.; Talice, M.; Juretić, F. Mitigating Thermal NOx by Changing the Secondary Air Injection Channel: A Case Study in the Cement Industry. *Fluids* **2020**, *5*, 220. [CrossRef]

21.　Edland, R.; Smith, N.; Allgurén, T.; Fredriksson, C.; Normann, F.; Haycock, D.; Johnson, C.; Frandsen, J.; Fletcher, T.; Andersson, K. Evaluation of NOx-Reduction Measures for Iron-Ore Rotary Kilns. *Energy Fuels* **2020**, *34*, 4934–4948. [CrossRef]

22.　Larsson, I.A.S.; Lindmark, E.M.; Lundström, T.S.; Nathan, G.J. Secondary Flow in Semi-Circular Ducts. *J. Fluids Eng.* **2011**, *133*. [CrossRef]

23.　Larsson, I.A.S.; Lindmark, E.; Lundström, T.S.; Marjavaara, B.D.; Töyrä, S. Visualization of Merging Flow by Usage of PIV and CFD with Application to Grate-Kiln Induration Machines. *J. Appl. Fluid Mech.* **2012**, *5*, 81–89. [CrossRef]

24.　Larsson, I.A.S.; Granström, B.R.; Lundström, T.S.; Marjavaara, B.D. PIV analysis of merging flow in a simplified model of a rotary kiln. *Exp. Fluids* **2012**, *53*, 545–560. [CrossRef]

25.　Larsson, I.A.S.; Lundström, T.S.; Marjavaara, B.D. Calculation of Kiln Aerodynamics with two RANS turbulence models and by DDES. *Flow Turbul. Combust.* **2015**, *94*, 859–878. [CrossRef]

26.　Larsson, I.A.S.; Lundström, T.S.; Marjavaara, B.D. The Flow Field in a Virtual Model of a Rotary Kiln as a Function of Inlet Geometry and Momentum Flux Ratio. *J. Fluids Eng.* **2015**, *137*, 101102. [CrossRef]

27.　Larsson, I.A.S.; Johansson, S.P.A.; Lundström, T.S.; Marjavaara, B.D. PIV/PLIF experiments of jet mixing in a model of a rotary kiln. *Exp. Fluids* **2015**, *56*, 111. [CrossRef]

28.　Larsson, I.A.S.; Lycksam, H.; Lundström, T.S.; Marjavaara, B.D. Experimental study of confined coaxial jets in a non-axisymmetric co-flow. *Exp. Fluids* **2020**, *61*, 1–17. [CrossRef]

29.　Larsson, I.A.S.; Ljung, A.L.; Marjavaara, B.D. Simulation of Thermal Effects on the Flow Field in a Pilot-Scale Kiln. *Min. Metall. Explor.* **2021**, *38*, 1487–1495. [CrossRef]

30.　Teng, Z.; Johansson, S.P.A.; Larsson, I.A.S.; Lundström, T.S.; Marjavaara, B.D. CFD Simulation of Jet Mixing with Asymmetric Co-flows in a Down-scaled Rotary Kiln Model. In Proceedings of the ASME 2016 International Mechanical Engineering Congress and Exposition, Phoenix, AZ, USA, 11–17 November 2016; Volume 7. [CrossRef]

31.　Teng, Z.; Larsson, I.A.S.; Lundström, T.S.; Marjavaara, B.D. The Effect of Reynolds Number on Jet in Asymmetric Co-Flows: A CFD Study. *Int. J. Chem. Eng.* **2018**, *2018*, 1572576. [CrossRef]

32. Boateng, A.A. *Rotary Kilns—Transport Phenomena and Transport Processes*, 1st ed.; Butterworth-Heinemann: Oxford, UK, 2008.
33. Pope, S.B. *Turbulent Flows*; Cambridge University Press: Cambridge, UK, 2000. [CrossRef]
34. Menter, F.R. Two-equation eddy-viscosity turbulence models for engineering applications. *AIAA J.* **1994**, *32*, 1598–1605. [CrossRef]
35. Menter, F.; Kuntz, M.; Langtry, R., Ten years of industrial experience with the SST turbulence model. In *Turbulence, Heat and Mass Transfer 4*; Hanjalic, K., Nagano, Y., Tummers, M., Eds.; Begell House, Inc.: Danbury, CT, USA, 2003.
36. Spalart, P.; Jou, W.H.; Strelets, M.; Allmaras, S. Comments on the Feasibility of LES for Wings, and on a Hybrid RANS/LES Approach. In Proceedings of the First AFOSR International Conference on DNS/LES, Ruston, LO, USA, 4–8 August 1997.
37. Strelets, M. Detached eddy simulation of massively separated flows. In Proceedings of the 39th Aerospace Sciences Meeting and Exhibit, Reno, NV, USA, 8–11 January 2001.
38. Ansys Inc. *Ansys CFX-Solver Theory Guide*; Release 12.1; Ansys Inc.: Canonsburg, PA, USA, 2009.
39. Larsson, S. The Fluid Dynamics of the Cold Flow in a Rotary Kiln. Ph.D. Thesis, Luleå University of Technology, Luleå, Sweden, 2014.
40. Edland, R.; Normann, F.; Allgurén, T.; Fredriksson, C.; Andersson, K. Scaling of Pulverized-Fuel Jet Flames That Apply Large Amounts of Excess Air—Implications for NOx Formation. *Energies* **2019**, *12*, 2680. [CrossRef]
41. Gunnarsson, A.; Andersson, K.; Adams, B.; Fredriksson, C. Full-scale 3D-modelling of the radiative heat transfer in rotary kilns with a present bed material. *Int. J. Heat Mass Transf.* **2019**, *147*, 118924. [CrossRef]
42. Gunnarsson, A.; Andersson, K.; Adams, B.R.; Fredriksson, C. Discrete-Ordinates Modelling of the Radiative Heat Transfer in a Pilot-Scale Rotary Kiln. *Energies* **2020**, *13*, 2192. [CrossRef]
43. Wiinikka, H.; Sepman, A.; Ögren, Y.; Lindblom, B.; Nordin, L.O. Combustion Evaluation of Renewable Fuels for Iron-Ore Pellet Induration. *Energy Fuels* **2019**, *33*, 7819–7829. doi: 10.1021/acs.energyfuels.9b01356. [CrossRef]
44. Koveria, A.; Kieush, L.; Boyko, M.; Yaholnyk, M.; Poliakova, N. Production of iron ore pellets by utilization of sunflower husks. *Acta Metall. Slovaca* **2021**, *27*, 167–171. [CrossRef]
45. Wang, S.; Guo, Y.; Liu, K.; Yang, Z.; Liu, Y.; Jiang, Y.; Chen, F.; Zheng, F.; Yang, L. The Deposit Formation Mechanism in Coal-Fired Rotary Kiln for Iron Ore Pellet Production: A Review. *Crystals* **2021**, *11*, 974. [CrossRef]
46. Lewis, A. Optimising air quality co-benefits in a hydrogen economy: A case for hydrogen-specific standards for NOx emissions. *Environ. Sci. Atmos.* **2021**, *1*, 201–207. [CrossRef]